Touchable Computing:
Computing-inspired Bio-detection

Yifan Chen*, *Senior Member, IEEE,* Shaolong Shi, Xin Yao, *Fellow, IEEE,* and Tadashi Nakano, *Member, IEEE*

Abstract—We propose a new computing-inspired bio-detection framework called touchable computing (TouchComp). Under the rubric of TouchComp, the best solution is the cancer to be detected, the parameter space is the tissue region at high risk of malignancy, and the agents are the nanorobots loaded with contrast medium molecules for tracking purpose. Subsequently, the cancer detection procedure (CDP) can be interpreted from the computational optimization perspective: a population of externally steerable agents (i.e., nanorobots) locate the optimal solution (i.e., cancer) by moving through the parameter space (i.e., tissue under screening), whose landscape (i.e., a prescribed feature of tissue environment) may be altered by these agents but the location of the best solution remains unchanged. One can then infer the landscape by observing the movement of agents by applying the "seeing-is-sensing" principle. The term "touchable" emphasizes the framework's similarity to controlling by touching the screen with a finger, where the external field for controlling and tracking acts as the finger. Given this analogy, we aim to answer the following profound question: *can we look to the fertile field of computational optimization algorithms for solutions to achieve effective cancer detection that are fast, accurate, and robust*? Along this line of thought, we consider the classical particle swarm optimization (PSO) as an example and propose the PSO-inspired CDP, which differs from the standard PSO by taking into account realistic *in vivo* propagation and controlling of nanorobots. Finally, we present comprehensive numerical examples to demonstrate the effectiveness of the PSO-inspired CDP for different blood flow velocity profiles caused by tumor-induced angiogenesis. The proposed TouchComp bio-detection framework may be regarded as one form of natural computing that employs natural materials to compute.

Index Terms—Touchable computing, computing-inspired bio-detection, metaheuristics, contrast-enhanced medical imaging, nanorobots, natural computing

*Y. Chen is with the Faculty of Science and Engineering and the Faculty of Computing and Mathematical Sciences, the University of Waikato, Hamilton, New Zealand, and with the Department of Electrical and Electronic Engineering, the Southern University of Science and Technology, Shenzhen, China (e-mail: yifan.chen@waikato.ac.nz).

S. Shi is with the Harbin Institute of Technology, Harbin, China, and with the Department of Electrical and Electronic Engineering, the Southern University of Science and Technology, Shenzhen, China (e-mail: 11649020@mail.sustc.edu.cn).

X. Yao is with the Department of Computer Science and Engineering, the Southern University of Science and Technology, Shenzhen, China, and with the School of Computer Science, the University of Birmingham, Birmingham, UK (e-mail: yaox@sustc.edu.cn).

T. Nakano is with the Graduate School of Frontier Biosciences, Osaka University, Osaka, Japan (e-mail: tadasi.nakano@fbs.osaka-u.ac.jp).

Touchable Communication (TouchComm): Communication-inspired Bio-delivery
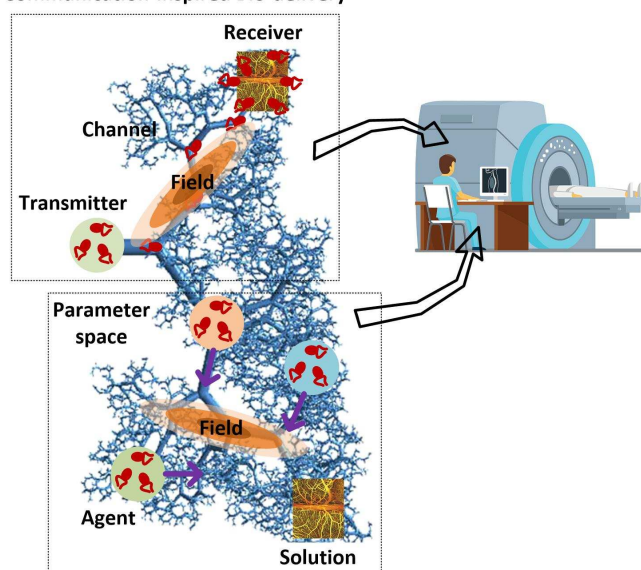
Touchable Computing (TouchComp): Computing-inspired Bio-detection

Fig. 1. Pictorial illustration of the communication-inspired bio-delivery and computing-inspired bio-detection procedures.

I. INTRODUCTION

A. Communication-inspired Bio-delivery

Communication theories can be employed as elegant mathematical tools for design and analysis of complex physical, chemical, and biological processes [1]. For example, in molecular communication (MC), a miniature transmitter emits molecules, which propagate and are eventually received by a miniature receiver [2]–[10]. The information can be encoded in either timing or concentration of molecules. The MC model is analogous to the drug delivery procedure (DDP), where transmission and reception correspond to drug injection and delivery, respectively. Channel is diffusion of drug particles in blood stream and signal is the concentration-time profile of drug. This approach revolutionizes DDP by utilizing performance measures traditionally only used in the communication field for optimal targeted therapies [11]–[19]. For example, by applying the queuing theory to model receptor saturation, thus treating it as a congestion problem in communication networks, the optimal drug release rate was estimated in [16] to guarantee that the desired fraction of receptors bound to drug molecules without drug overloading. By modeling the pharma-

cokinetics of DDP including the particle advection, diffusion, absorption, reaction, and adhesion through the abstraction of channel impulse response, the optimal drug injection rate was obtained in [14] by treating it as a channel inversion problem in communication systems.

Touchable communication (TouchComm) illustrated in Fig. 1 enhances the existing MC-inspired DDP by leveraging on the controllability and trackability of message carriers to reduce propagation delay, eliminate environmental uncertainty, and improve system practicality [15], [18]. The new framework can be used to characterize manoeuvrable drug delivery platforms in order to achieve high therapeutic index of nanocarriers in tumor regions. For example, magneto-aerotactic bacteria such as the *magnetococcus marinus* strain MC-1 were guided and tracked by a customized magnetic resonance imaging system for delivering drug-containing nanoliposomes to the disease site [20]. The term "touchable" emphasizes the framework's similarity to controlling by touching the screen with a finger, where the external field for controlling and tracking illustrated in Fig. 1 acts as the finger. Specifically, the in-messaging interfaces convert conventional electronic, magnetic, or optical signals used by the large-scale device into commands to which nanorobots respond by performing subsequent small-scale operations (e.g., through *magnetotaxis* directional control of MC-1 cells [20]), while the out-messaging interfaces convert motion signals generated by nanorobots (e.g., releasing, swimming, and targeting of nanorobots) to externally detectable and interpretable messages [21]. Contrast-enhanced microwave imaging can be employed as the out-messaging interface, where the cargo attached to nanorobots is a microwave contrast agent such as carbon nanotubes, ferroelectric nanoparticles, or magnetic nanoparticles, which can also be employed as a therapeutic agent [22]–[26]. Subsequently, the contrast-enhanced imaging technique has been applied for estimation of pharmacokinetics in the DDP, where the information-theoretic criteria [22] have been employed to determine the drug disposition in tumor [18]. This estimation step provides exact knowledge about the vascular channel specific to the individual patient and the DDP undergone, thereby alleviating the issue of a wide variety of vascular systems across different patients. Several strategies for optimal targeted therapies have been proposed from the communication waveform design perspective, which are based on minimization of residual drug molecules at the end of each therapeutic session, maximization of duration when the drug intensity is above a prespecified threshold during each therapeutic session, and minimization of average rate that a therapeutic operation is not received correctly at tumor [18]. These three criteria are inspired by the communication performance measures of inter-symbol interference, non-fade duration, and bit error rate, respectively.

B. Computing-inspired Bio-detection

In this paper, we extend the TouchComm concept to the computing domain and set out the fundamentals of computing-inspired bio-detection, dubbed touchable computing (Touch-Comp). The TouchComp model is also depicted in Fig. 1. The best solution is the cancer to be detected; the parameter space representing all possible solutions is the tissue region at high risk of malignancy; the externally manoeuvrable agents are nanorobots such as MC-1 bacteria, The agents (i.e., nanorobots) locate the optimal solution (i.e., cancer) by moving through the parameter space (i.e., high-risk tissue) under the guidance of an exterior steering field as shown in Fig. 1. The landscape of the solution space may be altered by agents due to the *natural computing* feature of TouchComp (i.e., employing natural materials such as nanorobots to compute) where agents interact with the solution space (i.e., nanorobots undergo physical, chemical, and biological reactions in the *in vivo* environment). This is in contrast to the classical *mathematical computing* using ideal non-interacting agents. An external observer can then infer the space by monitoring the movement of agents, which is called "seeing-is-sensing" in [27]. Provided with this analogy, a wide variety of computational techniques can thus be applied to the design of optimal cancer detection procedures (CDPs). To elaborate on the key concepts of TouchComp, the metaheuristic particle swarm optimization (PSO) [28] is used to inspire the CDP, assuming that the landscape of the tissue region under surveillance is unknown, nonlinear, and multimodal. The moves of nanorobots at each step are according to the mathematical formulae governing the iterative updates of agents' positions and velocities in the PSO but taking into account the physical constraints in realistic *in vivo* environments. Nevertheless, other optimization strategies can also be utilized given the specific use case under consideration. It is worth noting that TouchComp is an approach for optimized CDP inspired by a computational algorithm, but TouchComp itself is not meant to be a new bio-inspired computing technique or an improved metaheuristic. Instead, given the intriguing analogy between computation and bio-detection, we attempt to answer the following question: can we look to the fertile field of computational algorithms for solutions to achieve effective cancer detection that are fast, accurate, and robust?

Some preliminary results have been presented in [27], which however does not explicitly formulate the problem from the computing-inspired bio-detection perspective. Furthermore, the spatial distribution of a cancer in the tissue region is assumed to be known *a priori* from a lower-resolution tomographic image. Hence, in [27] the optimal surveillance path of nanorobots can be planned beforehand based on the classical detection theory without resorting to evolutionary computation.

C. Organization of the Paper

The paper is organized as follows. In Section II, we set out the fundamentals of the TouchComp framework. Subsequently, we establish the correspondence between bio-detection and computation in Section III. Three representative objective functions are then employed to describe reduced blood flow velocities in the cancerous tissue induced by tumor angiogenesis [29]–[31], which are imprinted on the invasion-percolation-based network model that mimics the normal vasculature and the irregular patterns found in tumors [32]–[34]. In Section IV, we propose the PSO-inspired CDP following from the
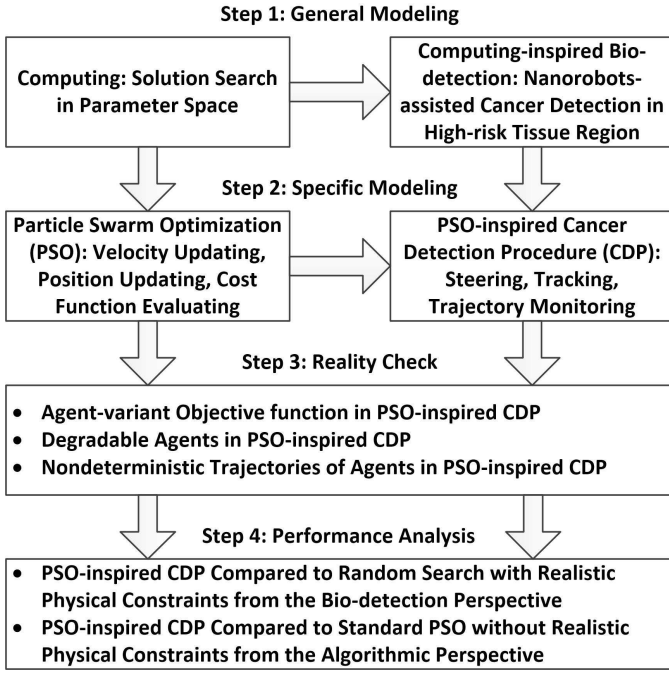
Step 1: General Modeling

Computing: Solution Search in Parameter Space	**Computing-inspired Bio-detection: Nanorobots-assisted Cancer Detection in High-risk Tissue Region**

Step 2: Specific Modeling

Particle Swarm Optimization (PSO): Velocity Updating, Position Updating, Cost Function Evaluating	**PSO-inspired Cancer Detection Procedure (CDP): Steering, Tracking, Trajectory Monitoring**

Step 3: Reality Check

- Agent-variant Objective function in PSO-inspired CDP
- Degradable Agents in PSO-inspired CDP
- Nondeterministic Trajectories of Agents in PSO-inspired CDP

Step 4: Performance Analysis

- PSO-inspired CDP Compared to Random Search with Realistic Physical Constraints from the Bio-detection Perspective
- PSO-inspired CDP Compared to Standard PSO without Realistic Physical Constraints from the Algorithmic Perspective

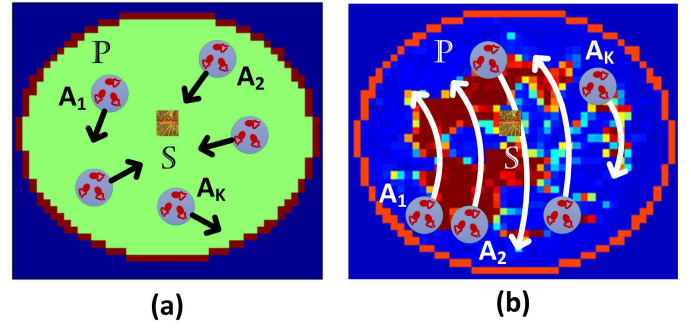Fig. 2. Flowchart of the TouchComp strategy.

(a)   **(b)**

Fig. 3. (a) Agents $A_1 \sim A_K$ spread out and search for solution $\mathbb{S}$ in random locations following some metaheuristics when there is no prior knowledge about the parameter space $\mathbb{P}$; (b) agents $A_1 \sim A_K$ survey the parameter space $\mathbb{P}$ in a more coordinated and deterministic manner when the areas with high probabilities of finding solutions (regions in red) are known *a priori*.

problem setting presented in Sections II and III. In Section V, the realistic physical constraints of the PSO-inspired CDP as compared to the standard PSO are discussed. In Section VI, we provide numerical examples to demonstrate the effectiveness of the proposed framework. Finally, some concluding remarks are drawn in Section VII.

II. GENERAL FRAMEWORK OF TOUCHCOMP

The general framework of TouchComp for computing-inspired bio-detection is illustrated in Fig. 2, which encompasses the following key steps.

- *Step 1 (General Modeling)*: Formulating the process of nanorobots-assisted cancer detection in high-risk tissue regions as a stylized representation of the general problem of agents-aided solution-searching in the parameter space.
- *Step 2 (Specific Modeling)*: Considering a specific computational optimization algorithm $\mathcal{A}$, which is the PSO in the current work, and mapping $\mathcal{A}$ onto the corresponding CDP $\mathcal{P}$. For example, the key operations in a standard PSO include velocity updating, position updating, and cost function evaluating, which correspond to steering, tracking, and trajectory monitoring in the PSO-inspired CDP.
- *Step 3 (Reality Check)*: Identifying the key physical constraints associated with $\mathcal{P}$ when applied in realistic *in vivo* environments, compared to the original algorithm $\mathcal{A}$ when applied in idealistic mathematical operations.
- *Step 4 (Performance Analysis)*: Evaluating the performance of $\mathcal{P}$ by comparing $\mathcal{P}$ to random search without implementing any optimization strategy from the cancer detection perspective (i.e., with physical imperfections), and comparing $\mathcal{P}$ to $\mathcal{A}$ from the algorithmic perspective

(i.e., without physical imperfections). In the latter case, $\mathcal{P}$ is regarded as a degenerate form of $\mathcal{A}$.

Following the "no free lunch" theorems [35], for certain types of cancer detection problems, CDPs derived from other optimization algorithms may perform better than the PSO-inspired CDP. An important future work built upon the current ground-laying model is thus to compare different CDPs derived from their corresponding computational techniques.

III. COMPUTING-INSPIRED BIO-DETECTION

We establish the correspondence between the agents-aided solution-searching process and the nanorobots-assisted cancer detection as stated in Step 1 of Fig. 2.

A. Problem Formulation

Consider a general parameter space $\mathbb{P}$ where K agents $A_1, A_2, \cdots, A_K$ are deployed to search for the best solution $\mathbb{S}$. The *agent-dependent* landscape is expressed as:

$$
\begin{aligned}
o\left(\vec{x}; A_k\right) &= o_{\mathrm{ms}}\left(\vec{x}; A_k\right) + o_{\mathrm{fit}}\left(\vec{x}; A_k\right) \\
&= o_{\mathrm{in}}(\vec{x}) + o_{\mathrm{ex}}\left(\vec{x}; A_k\right) + o_{\mathrm{fit}}\left(\vec{x}; A_k\right), \quad \vec{x} \in \mathbb{P},
\end{aligned}
\tag{1}
$$

where $o_{\mathrm{ms}}\left(\vec{x}; A_k\right)$ is the externally measurable objective function at location $\vec{x}$ for the kth agent A_k ($k = 1, 2, \cdots, K$), $o_{\mathrm{in}}(\vec{x})$ is the intrinsic objective function at $\vec{x}$ independent of the presence or absence of A_k, $o_{\mathrm{ex}}\left(\vec{x}; A_k\right)$ is the extrinsic disturbance caused to landscape due to the interaction between A_k and the parameter space $\mathbb{P}$, and $o_{\mathrm{fit}}\left(\vec{x}; A_k\right)$ is the correction factor accounting for the fitness of A_k, $\mathcal{F}_{A_k}$, due to its degradation in $\mathbb{P}$. For a meaningful optimization process, it is assumed that regardless of any variation caused by agents to the landscape, the location of the globally optimal solution $\mathbb{S}$, $\vec{x}^\star$, remains unchanged. It is worth noting that there may be alternative forms of agent-dependent landscapes other than (1) for which the general principles presented in the current work still hold. Furthermore, we focus on the scenario where there is only one best solution and leave the more complicated multiple-solutions problem for future investigation.

Subsequently, depending on availability of the prior knowledge about the parameter space, individual agents may spread

out and begin their search in random locations following some metaheuristics or probe the field in a more coordinated and deterministic manner [27] as illustrated in Fig. 3(a) and 3(b), respectively. Eventually, the whole field is surveyed and the agents end up swarming around the location of the globally optimal solution. The sequence of the optimization process is as follows.

1) *Initialization.* Agents are deployed in the parameter space $\mathbb{P}$ at the starting time t_0 with initial locations $\vec{x}_1(t_0), \vec{x}_2(t_0), \cdots, \vec{x}_K(t_0)$. For example, $\vec{x}_k(t_0) (k = 1, 2, \cdots, K)$ may be uniformly distributed in $\mathbb{P}$ if the landscape (objective function) of $\mathbb{P}$ is completely unknown. On the other hand, $\vec{x}_k(t_0)$ may be placed in areas with high possibility of achieving the best solution or areas suitable for initial agent deployment, which are known *a priori*. The initial speed of A_k is $v_k(\vec{x}_k(t_0))$. Furthermore, we define the fitness of A_k to be the duration when A_k has been interacting with $\mathbb{P}$. This is because the deterioration level of agents increases with the time of operation, which results in gradual reduction in their speed (e.g., the velocity of bacterial nanorobots decreased with respect to the immersion time in the blood medium due to high blood temperature [36], [37]). The initial fitness $\mathcal{F}_{A_k}(t_0) = 0$.

2) *Controlling.* Each agent trajectory is influenced by two factors: an angle deviation $\phi_{\mathbb{F}}(\vec{x}_k(t_0))$ relative to a principal axis denoting the external steering force $\mathbb{F}$ upon A_k at $\vec{x}_k(t_0)$, and an angle deviation $\phi_{\mathbb{P}}(\vec{x}_k(t_0))$ relative to the steering field summarizing all directional effects due to interaction between A_k and $\mathbb{P}$ at $\vec{x}_k(t_0)$. The next locations of all agents at time instant t_1 are then updated according to:

$$
\begin{aligned}
\vec{x}_k(t_1) &= \vec{x}_k(t_0) + d_k(t_0, t_1)\, \vec{u}_{\angle \phi_{\mathbb{F}}(\vec{x}_k(t_0)) + \phi_{\mathbb{P}}(\vec{x}_k(t_0))} \\
&= \vec{x}_k(t_0) \\
&+ \sum_{l=1}^{L_k(t_0,t_1)} v_k(\vec{x}_k(t_0))\, \zeta_{t_{k,l}}(t_0,t_1)\, \vec{u}_{\angle \phi_{k,l}(t_0,t_1)},
\end{aligned}
\tag{2}
$$

where $d_k(t_0, t_1)$ is the displacement length from $\vec{x}_k(t_0)$ to $\vec{x}_k(t_1)$, $\vec{u}_{\angle \phi}$ is a unit vector with angle ϕ, $L_k(t_0, t_1)$ is the number of piecewise-linear sections along the trajectory of A_k from $\vec{x}_k(t_0)$ to $\vec{x}_k(t_1)$ in the parameter space, $\zeta_{t_{k,l}}(t_0, t_1)$ is the traveling time of the lth linear section satisfying $\sum_{l=1}^{L_k(t_0,t_1)} \zeta_{t_{k,l}}(t_0, t_1) = t_1 - t_0 = \Delta t$ with Δt being the constant interval of the controlling cycle, and $\phi_{k,l}(t_0, t_1)$ is the direction of the lth linear section.

3) *Tracking.* In contrast to the traditional mathematical computing where an exact knowledge on the updated locations of agents is available, the new positions of agents need to be estimated for natural computing. Suppose that the estimated location is $\vec{x}'_k(t_1)$. The estimated velocity of agent A_k is given by $[\vec{x}'_k(t_1) - \vec{x}_k(t_0)]/\Delta t$. The updated fitness of A_k is then $\mathcal{F}_{A_k}(t_1) = \Delta t$. In general, the tracking time is much shorter than the controlling time during each iteration. Thus, the iteration period can be approximated as Δt.

4) *Decision-making and Iterating.* Following from (1), the objective functions obtained by all agents are computed. If certain stopping criteria are met, the solution $\mathbb{S}$ is found. Otherwise, new guiding forces denoted by directions $\phi_{\mathbb{F}}(\vec{x}_k(t_1))$, which can be approximated by $\phi_{\mathbb{F}}(\vec{x}'_k(t_1))$, are generated for all agents by following some metaheuristics. The displacement vector $d_k(t_1, t_2)\, \vec{u}_{\angle \phi_{\mathbb{F}}(\vec{x}_k(t_1)) + \phi_{\mathbb{P}}(\vec{x}_k(t_1))}$ determines the subsequent location of A_k as described in (2). In case that a specific agent A_κ fully degenerates in $\mathbb{P}$, a new agent is deployed in the initial deployment site to ensure that the total number of agents remains unchanged. Subsequently, the iteration continues.

The aforementioned computing process is analogous to the nanorobots-assisted CDP as detailed below.

1) The parameter space $\mathbb{P}$ is the high-risk tissue region under surveillance and the solution $\mathbb{S}$ is the tissue malignancy to be detected.

2) Each agent is a swarm of contrast-medium-appended nanorobots, which are injected into the tissue region and monitored by an external system *via* the in-messaging and out-messaging interfaces. The in-messaging interface controls the release of nanorobots at a specified location and time and initializes the CDP. This interface also influences the movement of nanorobots in the *in vivo* environment *via* magnetotaxis where an external magnetic field $\mathbb{F}$ is generated to steer the nanorobots [20], [36]. The out-messaging interface tracks the release of nanorobots and their path through a contrast-enhanced medical imaging modality [22], [23].

3) In normal tissues, the hemodynamic function of vasculature is to increase the cross-sectional area available to the blood flow in order to bring its velocity down to a level sufficiently low to permit the exchange of metabolic products across the capillary wall. Furthermore, for tumor tissues, microvascular blood velocity is significantly lower than the normal region due to the abnormal structure of the tumor vascular wall [38]. This phenomenon has been observed for cancer cells in the visceral pleura [30], malignant gliomas [33], and pancreatic tumors [31]. Given the velocity gradient introduced by tumor angiogenesis, the intrinsic objective function $o_{\text{in}}(\vec{x})$ can be set to be the speed of contrast-medium-loaded nanorobot without any disturbance, and is equal to the velocity of blood flow in the tissue region under screening. Note that $o_{\text{in}}(\vec{x})$ is not a continuous function over $\vec{x}$, which is dependent on the underlying interconnected vascular network around the tumor as to be discussed in Section III-B.

4) The extrinsic disturbance $o_{\text{ex}}(\vec{x})$ is the change to the speed of contrast-medium-loaded nanorobots caused by the biological and chemical interaction between the contrast medium/nanorobot and the human vasculature at location $\vec{x}$. This is of particular interest when nanorobots encounter with the tumor, the contrast medium molecules will be removed and get assimilated into the tumor. As the external system tracks the movement of contrast medium instead of nanorobots, the agent would appear to stop
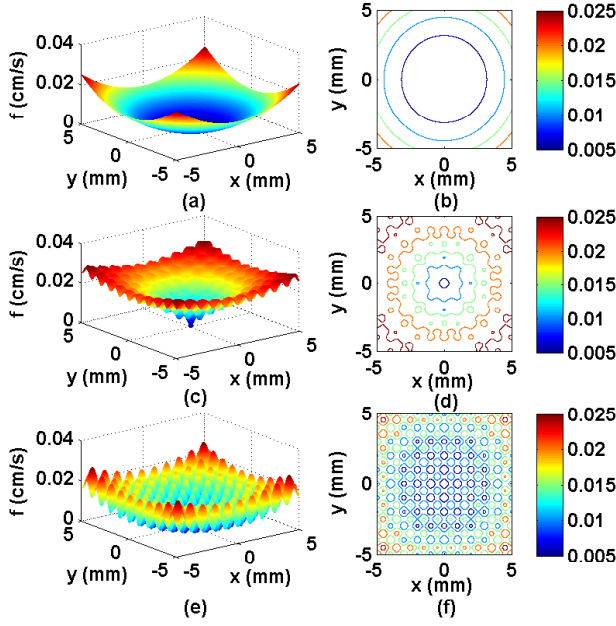
Fig. 4. Blood flow velocity profiles: (a) Sphere function and (b) its contour plot; (c) Ackley function and (d) its contour plot; (e) Rastrigin function and (f) its contour plot.

moving and $o_{ex}(\vec{x}; A_k) = -o_{in}(\vec{x})$. Otherwise, chemical reactions between nanorobots and blood medium will generate energy, and the flagellar bundles of nanorobots will provide a thrust force to propel the nanorobots. Initial experiments conducted in human blood at $37°$ showed that the velocity of the MC-1 bacteria decreased with the immersion time. For simplicity, the following model is assumed based on the measured velocity-time profile of MC-1 [15]:

$$o_{ex}(\vec{x}; A_k) = V \exp\left(-\frac{\mathcal{F}_{A_k}}{\tau}\right), \quad (3)$$

where V is the theoretical initial speed of agent and τ determines the decaying rate.

5) The correction factor $o_{fit}(\vec{x}; A_k)$ compensates for decrease in the speed of nanorobots formulated in (3). If there is an abrupt drop in the observed speed of nanorobots $o_{ms}(\vec{x}; A_k)$, which is below a certain threshold given by the minimum blood flow velocity in normal tissues, it is supposed that a tumor is detected and $o_{fit}(\vec{x}; A_k)$ is set to be 0. Otherwise, $o_{fit}(\vec{x}; A_k)$ is given by:

$$o_{fit}(\vec{x}; A_k) = V - V \exp\left(-\frac{\mathcal{F}_{A_k}}{\tilde{\tau}}\right), \quad (4)$$

assuming that the initial speed of agents can be measured accurately but only an estimated degeneration constant $\tilde{\tau}$ is available. Hence, the landscape can be written as:

$$o(\vec{x}; A_k) =$$
$$\begin{cases} 0, & \text{Tumor detected} \\ o_{in}(\vec{x}) + V + V\left[\exp\left(-\frac{\mathcal{F}_{A_k}}{\tau}\right) - \exp\left(-\frac{\mathcal{F}_{A_k}}{\tilde{\tau}}\right)\right], & \\ & \text{Tumor not detected.} \end{cases} \quad (5)$$

B. Blood Flow Velocity Profiles

To the best of our knowledge, there has not been any quantitative velocity model of tumor-angiogenesis-induced blood flow in the existing literature except for the consistent qualitative observation that tumor tissue reduces microvascular blood velocity [30], [31], [33], [38]. Hence, for the initial investigation we will consider some representative objective functions in computational optimization to evaluate the cancer detection performance of TouchComp, such as convergence, precision, and robustness. As illustrated in Fig. 4, the following three landscapes (scaled and shifted for fair comparison) with different levels of optimization complexity [39] are employed to represent the blood flow velocity profile for an early-stage tumor relevant to the current application scenario, which is the intrinsic objective function $o_{in}(\vec{x})$ (cm/s), where $\vec{x} = (x, y)$ in mm. The search domain is $-5\text{mm} \leq x, y \leq 5\text{mm}$. These functions have been routinely included in almost all catalogs of standard test problems.

1) *Sphere Function:*

$$o_{in}(\vec{x}) = \begin{cases} 0, & \sqrt{x^2 + y^2} \leq 0.1 \\ 0.0005\left(x^2 + y^2\right), & \text{Otherwise.} \end{cases} \quad (6)$$

As shown in Fig. 4(a) and 4(b), this function represents the situation that the core of an early-stage cancer, denoted by a circle of radius 0.1mm centered at the origin, yields abrupt decrease of the speed of contrast medium. The speed of blood flow decreases smoothly as the vessel becomes farther away from the tumor. The Sphere model is a simple function with one local optimum, which is therefore also global.

2) *Ackley Function:*

$$o_{in}(\vec{x}) =$$
$$\begin{cases} 0, & \sqrt{x^2 + y^2} \leq 0.1 \\ -0.04 \exp\left[-0.2\sqrt{0.5\left(x^2 + y^2\right)}\right] & \\ -0.002 \exp\left\{0.5\left[\cos(2\pi x) + \cos(2\pi y)\right]\right\} & \\ +0.00175e + 0.035, & \text{Otherwise.} \end{cases} \quad (7)$$

As shown in Fig. 4(c) and 4(d), this function represents the situation that the speed of blood flow reduces gradually with some ripples as the distance between blood vessels and tissue malignancy increases and becomes zero at the central region of the early-stage tumor, which is represented by a circle of radius 0.1mm centered at the origin. The Ackley model has an exponential term that covers its surface with numerous local minima. The complexity of this function is moderate.

3) *Rastrigin Function:*

$$o_{in}(\vec{x}) =$$
$$\begin{cases} 0, & \sqrt{x^2 + y^2} \leq 0.1 \\ \frac{1}{150} + \frac{1}{3000} & \\ \times\left[x^2 - 10\cos(2\pi x) + y^2 - 10\cos(2\pi y)\right], & \\ & \text{Otherwise.} \end{cases} \quad (8)$$

As shown in Fig. 4(e) and 4(f), this function represents the situation that there are a large number of localized areas with decreased blood flow velocity. The central
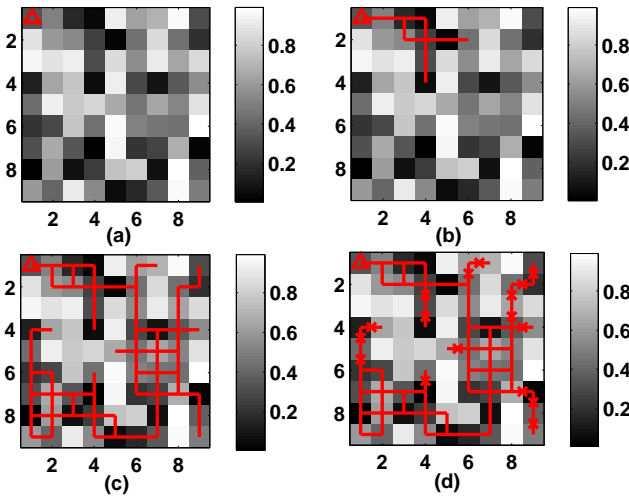
Fig. 5. Illustration of an invasion percolation algorithm: (a) initial condition, (b) after 10 growth steps, and (c) after 70 growth steps; (d) pruning of vessels with zero blood flow marked by crosses after 70 growth steps.

Fig. 6. Simulated multi-layer vascular network for the blood flow velocity profiles in (6)-(8). The vasculature is created by regular space-filling arrays with different microvascular densities representing normal and peritumoral tissues and invasion-percolation-based structure representing tumor tissue with a reduced microvascular density. The tumor center is denoted by the red circle.

region of the early-stage cancer is located at the origin, where the speed of contrast agent reduces to zero. The Rastrigin model is the most difficult function to optimize among these three test problems due to a much higher multimodality and the absence of velocity gradient generated by tumor angiogenesis.

C. Vascular Network Models

The vascular topology deviates significantly from a tree structure in tumors. Fractal geometry is well suited to quantify the tumor morphological characteristics, which have been routinely used by pathologists to describe the irregularity of tumor vascular growth [34]. Typical skeletonized images of various classes of vascular networks demonstrate that normal capillaries produce essentially two-dimensional patterns such that they are almost uniformly distributed to ensure adequate oxygen transportation throughout the tissue [32]–[34]. On the other hand, tumor vessels have a profound sort of tortuosity with many smaller bends on each larger bend, which yields fractal dimensions of 1.89 ± 0.04 [32]–[34]. Furthermore, the microvascular density in the peritumoral region increases due to the supply of growth factors from the tumor and reduces in the tumor center due to a combination of severely reduced blood flow and solid stress exerted by the tumor [40].

In modeling microvasculature, it is a common practice to restrict the vessels to run only parallel to the coordinate axes [32]–[34], [40]–[43]. We assume that the normal tissue is regularly vascularized, which results in a homogeneous capillary network with a given microvascular density determined by intercapillary distance. The density increases at the tumor periphery. On the other hand, the fractal dimensions of tumor vasculature suggest that the tortuous vessels and a wide range of avascular spaces found in tumors are better represented by invasion percolation, which is a well-known statistical growth process governed by local substrate properties. The com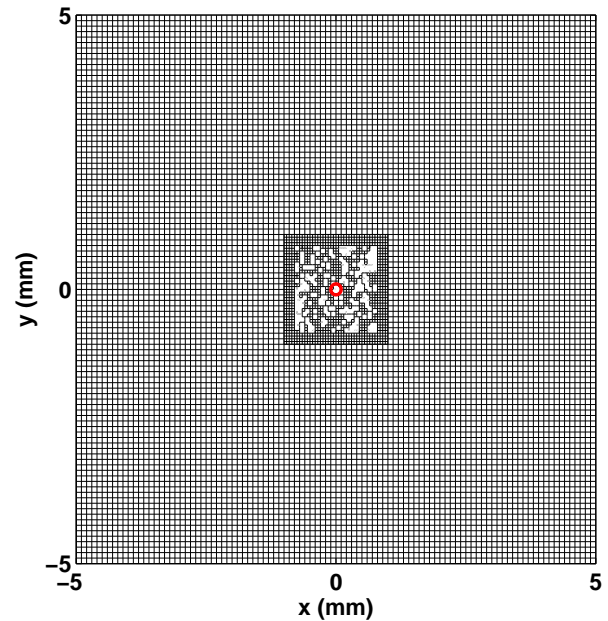putational model begins with a square lattice of discrete points that represent potential paths of vascular growth. Invasion percolation is implemented by first assigning uniformly distributed random values of strengths to each point on the underlying lattice. Starting at an arbitrary site the network occupies the lattice point adjacent to the current site that has the lowest strength. Growth is iterated until the desired lattice occupancy is reached. Blood vessels are assumed to connect all adjacent occupied lattice points. Blood is supplied at the starting entry point and withdrawn from a prescribed exit point. The network is then pruned to retain only those parts of the network with nonzero blood flow, leaving the backbone of the percolation cluster. The simulated networks may be matched with real tumor vasculature by considering the fractal dimensions, which can be achieved by selecting appropriate occupancy levels. Following [33], the fractal dimensions are around 1.6, 1.8, 1.9, and 2.0 for 40, 60, 80, and 100% occupancy on the backbone, respectively. Fig. 5(a)-(c) depict an invasion percolation procedure at the initial condition, after 10 growth steps, and after 70 growth steps, respectively. Fig. 5(d) shows the backbone of the percolation cluster after pruning the vessels with zero blood flow. Fig. 6 illustrates a simulated multi-layer vascular network for the blood flow velocity profiles in (6)-(8), created by regular space-filling arrays with different microvascular densities representing normal and peritumoral tissues and invasion-percolation-based structure representing tumor tissue. The intercapillary distances are $100\mu m$ and $50\mu m$ for normal and tumoral tissues, respectively [33]. The level of occupancy on the lattice is chosen to be 60% before pruning [33].

In the absence of detailed information on the diameters

of vessels, the viscosity of blood, and the applied blood pressure for tumor vessels and normal capillaries near the tumor, we simply imprint the velocity profiles in (6)-(8) on the vascular networks generated in Fig. 6. The two-dimensional lattice network is supposed to be comprised of straight, rigid cylindrical capillaries that join adjacent nodes [33], [42]. For each capillary element, the elemental flow rate in the capillary is assumed to follow Poiseuille's law, which forms a useful starting point for the development of more sophisticated models in future [33], [42]. At each node, a number of capillary elements come together and mass conservation means that the sum of all flows at each node must add up to zero. The blood inflow and outflow are assumed to be in the bottom left and top right, respectively, where prescribed pressures are set.

IV. PSO-INSPIRED CDP

For illustration purpose, we look into the PSO-inspired CDP here as stated in Step 2 of Fig. 2, but the general framework can be applied to other CDPs derived from different optimization algorithms. The original PSO was inspired from the simulation of social behavior of flocking organisms, such as swarms of birds or fish schools [28]. It can be understood by imagining a swarm of birds that search for foods in an open field. Each bird can remember the location that it found the most foods, and share this information with its neighbors. As time goes on, the birds profit from the discoveries and previous experience of all other companions during the search for foods by exploring the field in this manner: continuously updating their speed and direction-of-travel depending on how successful at finding foods they have been in comparison to the rest of the swarm, and constantly checking the field they fly over against previously encountered locations of highest food concentration. Eventually, the whole field is probed and the birds end up swarming around the location with the globally highest concentration of foods. In the following, we will formulate the CDP as a stylized representation of the PSO algorithm.

Each aggregate of nanorobots, called agent, adjust its own swimming path according to its swimming experience as well as the experience of other agents. Let us represent the kth agent by the vector $\vec{x}_k$ and the globally best agent by the position vector $\vec{g}$. The best previous position of the kth agent is recorded and represented as $\vec{p}_k$, and the velocity of the kth agent is $\vec{v}_k$. Note that the vessel network used in the simulation procedure is a discontinuous two-dimensional grid; therefore all the position and velocity vectors are mapped to the vectors associated with the nearest blood vessel. The standard PSO algorithm is modified here to suit the CDP. Subsequently, the agents evolve according to the following equations [see also (2)]:

$$\vec{u}_{\angle\phi_{\mathbb{F}}(\vec{x}_k)} = \frac{w\vec{v}_k + c_1 r_1 \frac{\vec{p}_k - \vec{x}_k}{\Delta t} + c_2 r_2 \frac{\vec{g} - \vec{x}_k}{\Delta t}}{\left| w\vec{v}_k + c_1 r_1 \frac{\vec{p}_k - \vec{x}_k}{\Delta t} + c_2 r_2 \frac{\vec{g} - \vec{x}_k}{\Delta t} \right|}, \quad (9)$$

$$\vec{x}_k = \vec{x}_k + \sum_{l=1}^{L_k} v_k \zeta t_{k,l} \vec{u}_{\angle\phi_{k,l}}. \quad (10)$$

The index $k = 1, 2, \cdots, K$; w is the inertial weight; c_1 and c_2 are two positive constants; r_1 and r_2 are two random values in the range $[0, 1]$; and Δt is the iteration period. Eq. (9) is used to calculate the new steering field for the kth agent by taking into account three terms: the agent's previous velocity, the distance between its best previous and current positions, and the distance between the position of the best agent in the swarm and the kth agent's current position. The inertia weight w determines to what extent the agent remains along its original course unaffected by the pull of $\vec{p}_k$ or $\vec{g}$. It regulates the tradeoff between the exploration and exploitation abilities of the swarm. A large w tends to encourage global exploration as a result of the agent being less moved by the pull of $\vec{p}_k$ and $\vec{g}$, whereas a small one tends to facilitate local exploitation in that agents are rapidly pulled toward $\vec{p}_k$ and $\vec{g}$. A general rule of thumb suggests that it is better to initially set w to a large value, in order to make a better global exploration of the search space, and gradually decrease it to get finer solutions. c_1 and c_2 are scaling factors that determine the relative pull of $\vec{p}_k$ and $\vec{g}$. These are also referred to as the cognitive and social rates, respectively. c_1 determines how much the agent is influenced by the memory of its best location, and c_2 is a factor determining how much the agent is influenced by the rest of the swarm. As default values, $c_1 = c_2 = 2$ were proposed in [28]. Eq. (10) evaluates the updated position of the kth agent given the steering field $\mathbb{F}$ and the underlying vascular network. For the lattice-like vessel system described in Section III-C where the vessels run only parallel to the two coordinate axes, at each junction the agent can move in two possible directions, up and right, as the flow is from bottom left to top right. Nevertheless, there are some exceptions in certain sparse areas of the tumor vasculature where the agent can move in three different directions: up, left, and right. The agent will move towards the direction that has the smallest angle deviation from the steering field.

Finally, due to the practical constraint of the PSO-inspired CDP, the initial deployment region of all agents is confined within a small area, which is the injection site of nanorobots, instead of the entire solution space. To further ensure that all agents are always confined within the tissue region under screening, the replacement strategy is implemented: agents are allowed to swim without any physical constriction. However, any agent that travels outside the allowed searching region is abandoned, which will degrade in the human body without further maneuvering and tracking. A new agent is then generated in the deployment area by injecting an aggregate of nanorobots to ensure that the overall number of agents remains unchanged.

V. REALITY CHECK OF PSO-INSPIRED CDP

We identify three fundamental physical constraints associated with the PSO-inspired CDP that employs natural computing with reference to the standard PSO algorithm that applies mathematical computing, as stated in Step 3 of Fig. 2.

Firstly, in contrast to mathematical computing, the objective function in the PSO-inspired CDP is dependent on the state ("fitness") of agents during the solution-searching process as

shown in (5) and thus is agent-variant, which is caused by the random physical, chemical, and biological interactions between nanorobots and the human tissue. Different aggregates of nanorobots would experience slightly different blood flow velocity profiles even for the same tissue region screened. Nevertheless, it is assumed that such disturbance may affect the optimization process but not the location of the global optimum.

Secondly, agents in the PSO-inspired CDP may be consumed during operation due to their transient kinetics. For example, each aggregate of nanorobots may undergo three different types of consumption: diffusion loss introduced by concentration gradient, branching loss at each junction of the vascular network, and degeneration loss upon immersion in the blood medium [15]. On the other hand, agents in mathematical computing are idealized point particles with an infinite lifespan.

Thirdly, the exact solution-searching trajectories of agents in the PSO-inspired CDP cannot be determined *a priori* in a perfect manner due to imprecise steering and inaccurate tracking of nanorobots at the exterior monitoring system. Another practical constraint is the grid-like vascular network, which reduces the degrees-of-freedom of nanorobot movement [27]. This is in contrast to mathematical computing where the updating of agent positions in the parameter space at each iteration can be carried out perfectly.

These three conditions should be taken into account when evaluating the performance of the PSO-inspired CDP from the following two aspects. In terms of cancer detection, the PSO-inspired CDP should be compared to random search subject to all the physical imperfections. In terms of algorithmic superiority, the PSO-inspired CDP should be compared to the standard PSO, where the former is treated as a degenerate form of the latter.

VI. PERFORMANCE ANALYSIS

We use several numerical examples to carry out the performance analysis of the PSO-inspired CDP as stated in Step 4 of Fig. 2. The three blood flow velocity profiles presented in Section III-B and the vascular network model presented in Section III-C are applied to synthesize tumor angiogenesis with different levels of detection difficulty. For the current application, a small population size of 10 is selected to minimize any adverse effect resulting from the presence of nanorobots in the human body. c_1 and c_2 are both set to 2.0, and the inertial weight w is varied linearly from 0.9 to 0.4 over 60 iterations. The duration of each iteration is 5sec and therefore, the overall operational time over 60 iterations is 5min. The initial deployment region is given by $-5\text{mm} \leq x, y \leq -4\text{mm}$. The initial speed of nanorobots is assumed to be $V = 100\mu\text{m/s}$, consistent with the speed of magnetotactic bacteria reported in the literature [36]. The actual degeneration constant is set to be $\tau = 5\text{min}$.

Fig. 7(a) shows a typical curve of minimum outcomes obtained from the agents over multiple iterations for the Sphere velocity profile by using the PSO-inspired CDP. The corresponding final positions of agents are shown in Fig. 7(b).
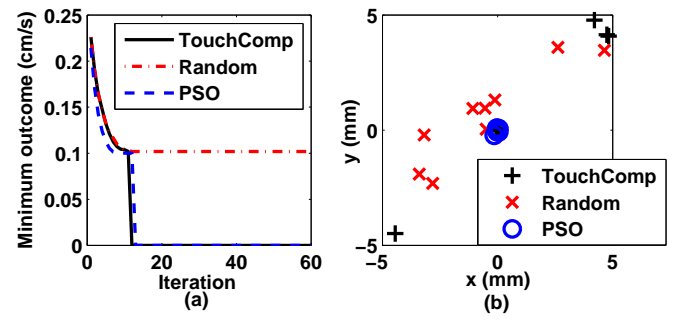

Fig. 7.　(a) Minimum outcomes obtained over iterations and (b) final positions of agents for the Sphere function. The TouchComp strategy is compared to random search and standard PSO from the cancer detection and algorithmic perspectives, respectively.
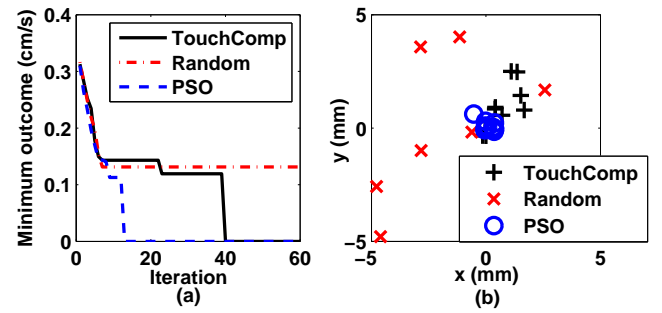

Fig. 8.　(a) Minimum outcomes obtained over iterations and (b) final positions of agents for the Ackley function. The TouchComp strategy is compared to random search and standard PSO from the cancer detection and algorithmic perspectives, respectively.
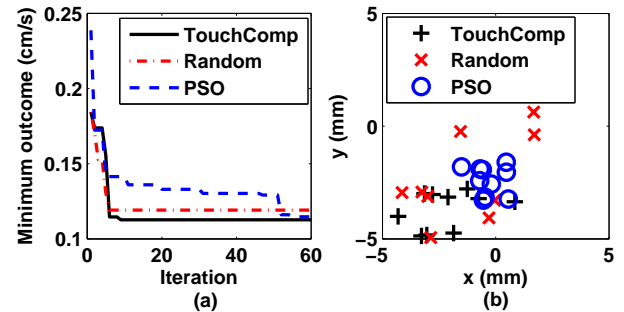

Fig. 9.　(a) Minimum outcomes obtained over iterations and (b) final positions of agents for the Rastrigin function. The TouchComp strategy is compared to random search and standard PSO from the cancer detection and algorithmic perspectives, respectively.

It can be seen that the cancer is successfully detected at the 12th iteration, and eventually some of the agents swarm around the center of the tumor at the origin. For comparison from the cancer detection perspective, we also show the results for the random search strategy without applying any metaheuristics under the same realistic constraints. In this case, the agents fail to detect the cancer at the end of the operation. Furthermore, for comparison from the algorithmic perspective, we present the results for the standard PSO without any physical imperfections. The target is detected at the 13th iteration and all
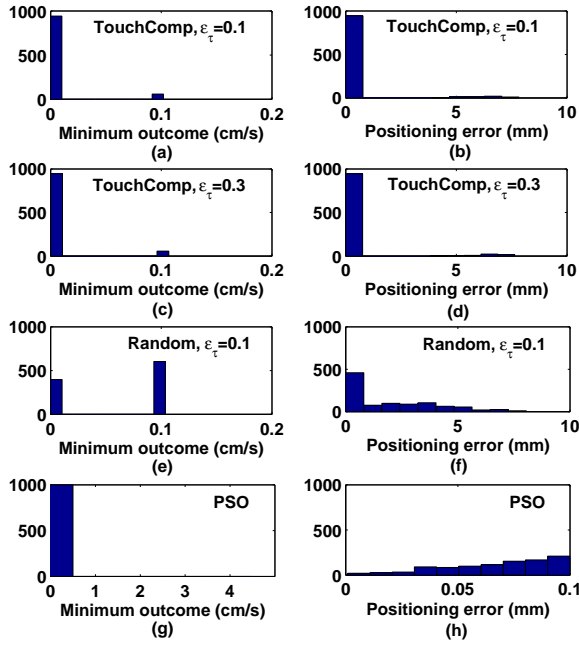
Fig. 10. Histograms of (a) minimum outcomes and (b) positioning errors for TouchComp with $\epsilon_\tau = 0.1$, histograms of (c) minimum outcomes and (d) positioning errors for TouchComp with $\epsilon_\tau = 0.3$, histograms of (e) minimum outcomes and (f) positioning errors for random search with $\epsilon_\tau = 0.1$, and histograms of (g) minimum outcomes and (h) positioning errors for standard PSO. The results are obtained over 1000 independent simulation runs for the Sphere function.
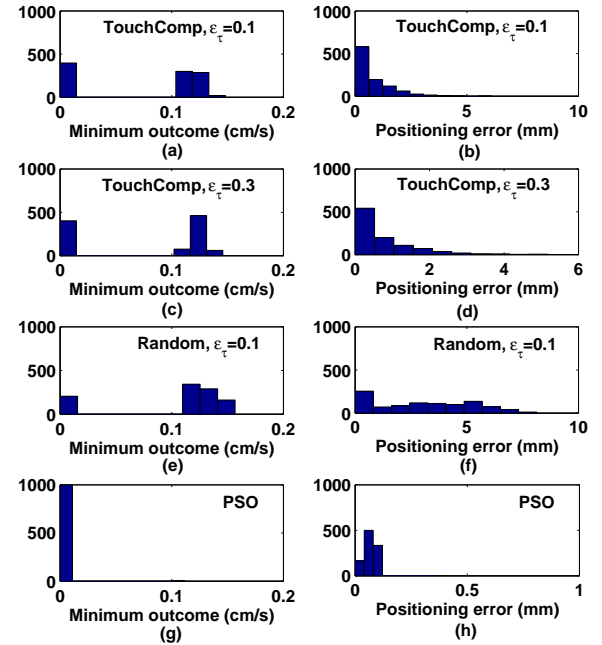

Fig. 11. Histograms of (a) minimum outcomes and (b) positioning errors for TouchComp with $\epsilon_\tau = 0.1$, histograms of (c) minimum outcomes and (d) positioning errors for TouchComp with $\epsilon_\tau = 0.3$, histograms of (e) minimum outcomes and (f) positioning errors for random search with $\epsilon_\tau = 0.1$, and histograms of (g) minimum outcomes and (h) positioning errors for standard PSO. The results are obtained over 1000 independent simulation runs for the Ackley function.

the agents swarm around the target at the end of operation, demonstrating superior performance over the PSO-inspired CDP.

Fig. 8 illustrates typical results of the Ackley function for the PSO-inspired CDP, random search, and standard PSO algorithms. Other than taking more iterations to find the cancer for the PSO-inspired CDP, similar observations with Fig. 7 can be made, which further verify the performance improvement achieved by TouchComp compared to random search for blood flows exhibiting velocity gradient generated by tumor angiogenesis. On the other hand, performance degradation of TouchComp compared to the original PSO is also found for the Ackley model.

Fig. 9 depicts typical detection outcomes of the Rastrigin function for all the three strategies. As can be seen from Fig. 9(a), all the algorithms fail to detect the tumor at the end of the operation due to the much higher multimodality and the absence of velocity gradient towards the cancerous site.

To provide statistical analysis of the robustness and precision of the PSO-inspired CDP, we have carried out 1000 independent simulation runs. Fig. 10(a) and 10(b) show the histograms of the minimum outcomes and positioning errors (defined as the distance between the origin and the location of the best agent in the swarm at the end of 60 iterations) for the Sphere function with an estimation error of the nanorobot degeneration constant, $\epsilon_\tau = 1 - \tilde{\tau}/\tau = 0.1$ [see also Eq. (5)]. The histograms of these two metrics for the PSO-inspired CDP

with $\epsilon_\tau = 0.3$, random search with $\epsilon_\tau = 0.1$, and standard PSO are shown in Fig. 10(c)-(d), 10(e)-(f), and 10(g)-(h), respectively. As shown in Fig. 10(a) and 10(c), the TouchComp strategy achieves nearly 100% of cancer detection regardless of ϵ_τ. On the other hand, random search yields a detection rate of less than 50% as shown in Fig. 10(e). The superiority of TouchComp over random search can also be observed in Fig. 10(b) and 10(f), where the positioning errors in the latter case are scattered over a much wider range compared to the former case. In general, different estimation errors of the degeneration constant do not result in significant performance deterioration in TouchComp for the Sphere model. As shown in Fig. 10(g) and 10(h), the standard PSO results in better optimization outcomes than its derived CDP from the algorithmic aspect.

Fig. 11 presents the histograms of the minimum outcomes and the positioning errors for the Ackley model. It can be seen from Fig. 11(a), 11(c), and 11(e) that the detection rates for both the TouchComp and random search strategies are reduced by half compared to the Sphere model due to many local minima in the landscape of the Ackley function. Nevertheless, TouchComp significantly outperforms random search in terms of the detection probability (two times improvement). This phenomenon is also demonstrated in the histograms in Fig. 11(b), 11(d), and 11(f) for the positioning error. Similar to the Sphere model, the cancer detection process is robust against the estimation error ϵ_τ for the PSO-inspired CDP. The standard PSO, on the other hand, yields almost the same target detection

This article has been accepted for publication in a future issue of this journal, but has not been fully edited. Content may change prior to final publication. Citation information: DOI 10.1109/TNB.2017.2769162, IEEE Transactions on NanoBioscience

IEEE TRANSACTIONS ON NANOBIOSCIENCE, VOL. XX, NO. XX, MONTH 2017
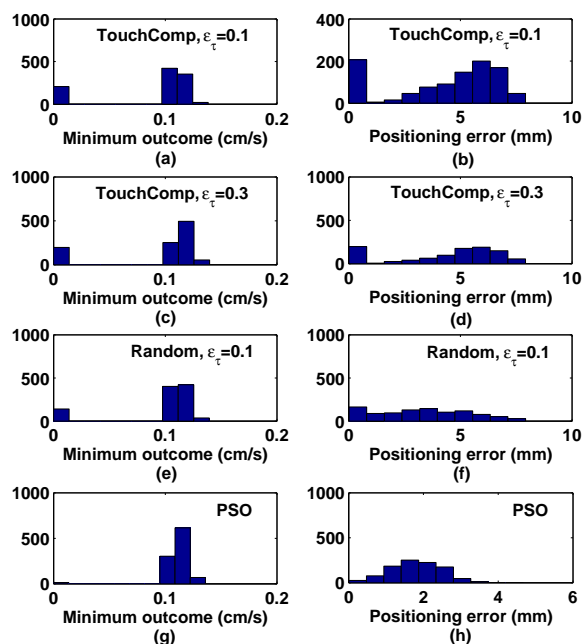
10

Fig. 12. Histograms of (a) minimum outcomes and (b) positioning errors for TouchComp with $\epsilon_\tau = 0.1$, histograms of (c) minimum outcomes and (d) positioning errors for TouchComp with $\epsilon_\tau = 0.3$, histograms of (e) minimum outcomes and (f) positioning errors for random search with $\epsilon_\tau = 0.1$, and histograms of (g) minimum outcomes and (h) positioning errors for standard PSO. The results are obtained over 1000 independent simulation runs for the Rastrigin function.

outcomes compared to the Sphere model and has significantly outperformed its derived CDP.

Finally, Fig. 12 illustrates the histograms of the minimum outcomes and the positioning errors for the Rastrigin function. Comparing Fig. 12 to Fig. 11 shows that, firstly, the detection rate and positioning accuracy become worse for the highly multimodal Rastrigin landscape as compared to the moderate Ackley problem and secondly, the TouchComp strategy still outperforms random search but their performance gap is closed further. Comparing Fig. 12(a) and 12(b) to Fig. 12(g) and 12(h) shows an interesting and somewhat unexpected phenomenon. The original PSO results in much worse detection performance compared to its derived CDP from the algorithmic perspective. This is plausibly due to the fact that a reduced degree-of-freedom of agent movement in TouchComp helps the agent to escape from the numerous local minima in the highly multimodal landscape.

VII. CONCLUSION

We have presented a novel computing-inspired nanorobots-assisted bio-detection framework, dubbed TouchComp. The proposed approach carries out optimized cancer detection inspired by computational algorithms. Specifically, we have also proposed the PSO-inspired CDP under the rubric of TouchComp. Numerical examples have demonstrated the effectiveness of the proposed methodology for various blood flow velocity profiles induced by tumor angiogenesis.

Future work may include extension of the framework to CDPs inspired by multi-solution or multi-objective optimizations when there are multiple tumors or different phenomena-of-interest in the tissue region under surveillance. It is also interesting to compare the performance of CDPs inspired by different metaheuristics. Moreover, it is important to examine further the impact of nanorobot nonidealities, such as finite lifespan, imprecise steering, and inaccurate tracking. Finally, empirical velocity models of tumor-angiogenesis-induced blood flow are required to justify further the clinical relevance of the proposed bio-detection strategy.

Nature's blueprints have inspired thrilling new science such as biologically inspired computing. It would be just as stimulating to look the other way by exploiting the best computing strategies for bio-detection.

REFERENCES

[1] I. S. Mian and C. Rose, "Communication theory and multicellular biology," *Integr. Biol.*, vol. 3, pp. 350–367, 2011.

[2] I. F. Akyildiz, F. Brunetti, and C. Blazquez, "Nanonetworks: A new communication paradigm," *Comput. Netw.*, vol. 52, pp. 2260–2279, Aug. 2008.

[3] M. J. Moore, T. Suda, and K. Oiwa, "Molecular communication: Modeling noise effects on information rate," *IEEE Trans. Nanobiosci.*, vol. 8, pp. 169–180, Jun. 2009.

[4] S. Hiyama and Y. Moritani, "Molecular communications: Harnessing biochemical materials to engineer biomimetic communication systems," *Nano Commun. Netw.*, vol. 1, no. 1, pp. 20–30, 2010.

[5] I. F. Akyildiz, J. M. Jornet, and M. Pierobon, "Nanonetworks: A new frontier in communications," *Commun. ACMs*, vol. 54, pp. 84–89, Nov. 2011.

[6] N. Farsad, A. W. Eckford, S. Hiyama, and Y. Moritani, "On-chip molecular communication: Analysis and design," *IEEE Trans. Nanobiosci.*, vol. 11, pp. 304–314, Sep. 2012.

[7] T. Nakano, A. W. Eckford, and T. Haraguchi, *Molecular Communications*, Cambridge University Press, 2013.

[8] T. Nakano, T. Suda, Y. Okaie, M. J. Moore, and A. V. Vasilakos, "Molecular communication among biological nanomachines: A layered architecture and research issues," *IEEE Trans. Nanobiosci.*, vol. 13, no. 3, pp. 169–197, Sep. 2014.

[9] Y. Chen, P. S. Anwar, L. Huang, and M. Asvial, "Characterizing nanoscale transient communication," *IEEE Trans. Nanobiosci.*, vol. 15, no. 3, pp. 218–229, 2016.

[10] N. Farsad, H. B. Yilmaz, A. Eckford, C.-B. Chae, and W. Guo, "A comprehensive survey of recent advancements in molecular communication," *IEEE Commun. Surveys Tuts.*, vol. 18, no. 3, pp. 1887–1919, 2016.

[11] Y. Chahibi, M. Pierobon, S. O. Song, and I. F. Akyildiz, "A molecular communication system model for particulate drug delivery systems," *IEEE Trans. Biomed. Eng.*, vol. 60, no. 12, pp. 3468–3483, Dec. 2013.

[12] Y. Chahibi and I. F. Akyildiz, "Molecular communication noise and capacity analysis for particulate drug delivery systems," *IEEE Trans. Commun.*, vol. 62, no. 11, pp. 3891–3903, Nov. 2014.

[13] Y. Chahibi, I. F. Akyildiz, S. Balasubramaniam, and Y. Koucheryavy, "Molecular communication modeling of antibody-mediated drug delivery systems," *IEEE Trans. Biomed. Eng.*, vol. 62, no. 7, pp. 1683–1695, July 2015.

[14] Y. Chahibi, M. Pierobon, and I. F. Akyildiz, "Pharmacokinetic modeling and biodistribution estimation through the molecular communication paradigm," *IEEE Trans. Biomed. Eng.*, vol. 62, no. 10, pp. 2410–2420, Oct. 2015.

[15] Y. Chen, P. Kosmas, P. S. Anwar, and L. Huang, "A touch-communication framework for drug delivery based on a transient microbot system," *IEEE Trans. Nanobiosci.*, vol. 14, no. 4, pp. 397–408, June 2015.

[16] M. Femminella, G. Reali, and A. V. Vasilakos, "A molecular communications model for drug delivery," *IEEE Trans. Nanobiosci.*, vol. 14, no. 8, pp. 935–945, Dec. 2015.

[17] U. A. K. Chude-Okonkwo, R. Malekian, and B. T. Sunil Maharaj, "Molecular communication model for targeted drug delivery in multiple disease sites with diversely expressed enzymes," *IEEE Trans. Nanobiosci.*, vol. 15, no. 3, pp. 230–245, Apr. 2016.

[18] Y. Chen, Y. Zhou, R. Murch, and P. Kosmas, "Modeling contrast-imaging-assisted optimal targeted drug delivery: A touchable communication channel estimation and waveform design perspective," *IEEE Trans. Nanobiosci.*, vol. 16, pp. 203–215, Apr. 2017.

[19] U. A. K. Okonkwo, R. Malekian, B. T. Maharaj, and A. V. Vasilakos, "Molecular communication and nanonetwork for targeted drug delivery: A survey," *IEEE Commun. Surveys Tuts.*, vol. PP, no. 99, pp. 1–1, 2017.

[20] O. Felfoul, M. Mohammadi, S. Taherkhani, and et al., "Magneto-aerotactic bacteria deliver drug-containing nanoliposomes to tumour hypoxic regions," *Nature Nanotechnology*, vol. 11, pp. 941–947, 2016.

[21] T. Nakano, S. Kobayashi, T. Suda, Y. Okaie, Y. Hiraoka, and T. Haraguchi, "Externally controllable molecular communication," *IEEE J. Sel. Areas Commun.*, vol. 32, no. 12, pp. 2417–2431, Dec. 2014.

[22] Y. Chen and P. Kosmas, "Detection and localization of tissue malignancy using contrast-enhanced microwave imaging: Exploring information theoretic criteria," *IEEE Trans. Biomed. Eng.*, vol. 59, pp. 766–776, Mar. 2012.

[23] Y. Chen, P. Kosmas, and S. Martel, "A feasibility study for microwave breast cancer detection using contrast-agent-loaded bacterial microbots," *Int. J. Antennas Propag.*, vol. 2013, Article ID 309703, 11 pages, http://dx.doi.org/10.1155/2013/309703.

[24] S. Semenov, N. Pham, and S. Egot-Lemaire, "Ferroelectric nanoparticles for contrast enhancement microwave tomography: Feasibility assessment for detection of lung cancer," in *Proc. World Congress on Medical Physics and Biomedical Engineering*, Munich, Germany, Sep. 2009.

[25] A. Mashal, B. Sitharaman, X. Li, P. K. Avti, A. V. Sahakian, J. H. Booske, and S. C. Hagness, "Toward carbon-nanotube-based theranostic agents for microwave detection and treatment of breast cancer: Enhanced dielectric and heating response of tissue-mimicking materials," *IEEE Trans. Biomed. Eng.*, vol. 57, pp. 1831–1834, Aug. 2010.

[26] G. Bellizzi, O. M. Bucci, and I. Catapano, "Microwave cancer imaging exploiting magnetic nanoparticles as contrast agent," *IEEE Trans. Biomed. Eng.*, vol. 58, pp. 2528–2536, Sept. 2011.

[27] Y. Chen, T. Nakano, P. Kosmas, C. Yuen, A. V. Vasilakos, and M. Asvial, "Green touchable nanorobotic sensor networks," *IEEE Commun. Mag.*, pp. 136–142, Nov. 2016.

[28] J. Kennedy, R. C. Eberhart, and Y. Shi, *Swarm Intelligence*, Elsevier, ISBN 978-1-55860-595-4, 2001.

[29] D. B. Ellegala, H. Leong-Poi, J. E. Carpenter, A. L. Klibanov, S. Kaul, M. E. Shaffrey, J. Sklenar, and J. R. Lindner, "Imaging tumor angiogenesis with contrast ultrasound and microbubbles targeted to alpha(v)beta3," *Circulation*, vol. 108, no. 3, pp. 336–341, 2003.

[30] Y. Wang, K. Iguchi, H. Ito, K. Ookawa, N. Kobayashi, R. Nakamura, Y. Goto, M. Sakai, S. Ishikawa, and M. Onizuka, "Blood flow velocity is reduced in a tumor micro-dissemination in the visceral pleura in anesthetized open-chest rat lung," *In Vivo*, vol. 23, pp. 291–296, 2009.

[31] G. Komar, S. Kauhanen, K. Liukko, M. Seppanen, S. Kajander, J. Ovaska, P. Nuutila, and H. Minn, "Decreased blood flow with increased metabolic activity: A novel sign of pancreatic tumor aggressiveness," *Clin. Cancer Res.*, vol. 15, no. 17, pp. 5511–5517, 2009.

[32] Y. Gazit, D. A. Berk, M. Leunig, L. T. Baxter, and R. K. Jain, "Scale-invariant behavior and vascular network formation in normal and tumor tissue," *Phys. Rev. Lett.*, vol. 75, no. 12, pp. 2428–2431, 1995.

[33] J. W. Baish, Y. Gazit, D. A. Berk, M. Nozue, L. T. Baxter, and R. K. Jain, "Role of tumor vascular architecture in nutrient and drug delivery: An invasion percolation-based network model," *Microvasc. Res.*, vol. 51, pp. 327–346, 1996.

[34] J. W. Baish and R. K. Jain, "Fractals and cancer," *Cancer Res.*, vol. 60, pp. 3683–3688, 2000.

[35] D. H. Wolpert and W. G. Macready, "No free lunch theorems for optimization," *IEEE Trans. Evol. Comput.*, vol. 1, no. 1, pp. 67–82, 1997.

[36] S. Martel, M. Mohammadi, O. Felfoul, Z. Lu, and P. Pouponneau, "Flagellated magnetotactic bacteria as contralled MRI-trackable propulsion and steering systems for medical nanorobots operating in the human microvasculature," *Int. J. Rob. Res.*, vol. 28, pp. 571–582, Apr. 2009.

[37] S. Martel, O. Felfoul, J.-B. Mathieu, A. Chanu, S. Tamaz, M. Mohammadi, M. Mankewich, and N. Tabatabaei, "MRI-based medical nanorobotic platform for the control of magnetic nanoparticles and flagellated bacteria for target interventions in human capillaries," *Int. J. Rob. Res.*, vol. 28, pp. 1169–1182, Sept. 2009.

[38] D. Fukumura and R. K. Jain, "Tumor microvasculature and microenvironment: targets for anti-angiogenesis and normalization," *Microvasc. Res.*, vol. 74, pp. 72–84, 2007.

[39] G. A. Ortiz, *Evolution Strategies (ES)*, Mathworks, 2014.

[40] D.-S. Lee, H. Rieger, and K. Bartha, "Flow correlated percolation during vascular remodeling in growing tumors," *Phys. Rev. Lett.*, vol. 96, no. 058104, 2006.

[41] A. R. A. Anderson and M. A. J. Chaplain, "Continuous and discrete mathematical models of tumor-induced angiogenesis," *Bull. Math. Biol.*, vol. 60, pp. 857–900, 1998.

[42] S. R. McDougall, A. R. A. Anderson, and M. A. J. Chaplain, "Mathematical modelling of flow through vascular networks: Implications for tumor-induced angiogenesis and chemotherapy strategies," *Bull. Math. Biol.*, vol. 64, pp. 673–702, 2002.

[43] A. Stephanou, S. R. McDougall, A. R. A. Anderson, and M. A. J. Chaplain, "Mathematical modelling of flow in 2D and 3D vascular networks: Applications to anti-angiogenic and chemotherapeutic drug strategies," *Math. Comput. Model.*, vol. 41, pp. 1137–1156, 2005.

Yifan Chen (M'06-SM'14) is a Professor of Engineering and the Associate Dean External Engagement for the Faculty of Science and Engineering and the Faculty of Computing and Mathematical Sciences in the University of Waikato, Hamilton, New Zealand. His current research interests include computing-inspired biosensing and communication-inspired biotransport, physics-based signal processing for microwave medical imaging, radiofrequency for body-centric imaging, sensing and communications, and propagation channel modeling. He is the Coordinator of the European FP7 "CoNHealth" project on intelligent medical ICT, an elected Working Group Co-leader of the European COST Action TD1301 "MiMed" project on microwave medical imaging, an Advisory Committee Member of the European Horizon 2020 "CIRCLE" project on molecular communications, an Associate Investigator of the New Zealand Consortium for Medical Device Technologies (CMDT) and MedTech Centre of Research Excellence (MedTech CoRE), a Voting Member of the IEEE Standards Development Working Group 1906.1 on nanoscale and molecular communications, an Editor for IEEE Communications Society Best Readings in Nanoscale Communication Networks and IEEE Access Special Section in Nano-antennas, Nano-transceivers, and Nano-networks/Communications, and a Vice Chair of the IEEE Communications Society Emerging Technologies Initiative for Molecular, Biological and Multi-Scale Communications. He also served as a General Chair, Technical Program Chair, Tutorial and Special Session Chair, and Local Organization Committee Chair for several premier IEEE conferences such as ICC, ICCE, ICCC, ICCS, APCAP, APEMC, etc. He is a Fellow of the Institution of Engineering and Technology (IET).

Shaolong Shi received the B.Sc. degree and M.Sc. degree in Control Science and Engineering from the Harbin Institute of Technology, Harbin, China, in 2014 and 2016, respectively. He is currently a Ph.D. student in the Department of Computer Science and Engineering, the Southern University of Science and Technology, Shenzhen, China, and the Harbin Institute of Technology. His current research interests include computing-inspired biosensing with application to cancer detection.

PLACE PHOTO HERE

Xin Yao (F'03) is a Chair Professor of Computer Science at the Southern University of Science and Technology, Shenzhen, China, and a Professor of Computer Science at the University of Birmingham, UK. He is an IEEE Fellow, and a Distinguished Lecturer of IEEE Computational Intelligence Society (CIS). His major research interests include evolutionary computation, ensemble learning, and their applications in software engineering. He has been working on multi-objective optimisation since 2003, when he published a well-cited EMO'03 paper on many objective optimisation. His research won the 2001 IEEE Donald G. Fink Prize Paper Award, 2010, 2016, and 2017 IEEE Transactions on Evolutionary Computation Outstanding Paper Awards, 2010 BT Gordon Radley Award for Best Author of Innovation (Finalist), 2011 IEEE Transactions on Neural Networks Outstanding Paper Award, and many other best paper awards. He received the prestigious Royal Society Wolfson Research Merit Award in 2012 and the IEEE CIS Evolutionary Computation Pioneer Award in 2013. He was the President (2014-15) of IEEE CIS, and the Editor-in-Chief (2003-08) of IEEE Transactions on Evolutionary Computation.

PLACE PHOTO HERE

Tadashi Nakano (M'05) received his Ph.D. degree in Information Systems Engineering from Osaka University, Japan, in 2002. He later worked in the Department of Computer Science, Donald Bren School of Information and Computer Sciences, University of California, Irvine, where he was a Postdoctoral Research Scholar from 2002 to 2007 and an Assistant Adjunct Professor from 2007 to 2009. From 2009 to 2013, he was an Associate Professor at the Graduate School of Engineering, Osaka University. Since 2013, he has been an Associate Adjunct Professor of the Institute of Academic Initiatives, Osaka University, and a Visiting Associate Professor of the Graduate School of Biological Sciences, Osaka University. He is currently serving as the Chair of the Emerging Technologies Initiative for Molecular, Biological and Multi-Scale Communications. He is also serving as an Associate Editor of IEEE Transactions on Molecular, Biological and Multi-scale Communications (T-MBMC), an Associate Editor of IEEE Transactions on NanoBioscience (TNB), and an Editor of Elsevier Nano Communication Networks. He has been engaged in research at the intersection of computer science and biology, including design, implementation, and evaluation of molecular communication systems, synthetic biological systems, and biologically inspired systems.